

FlowIBR: Leveraging Pre-Training for Efficient Neural Image-Based Rendering of Dynamic Scenes

Marcel Büsching¹
busching@kth.se

Josef Bengtson²
bjosef@chalmers.se

David Nilsson²
david.nilsson@chalmers.se

Mårten Björkman¹
celle@kth.se

¹KTH Royal Institute of Technology

²Chalmers University of Technology

Abstract

We introduce a novel approach for monocular novel view synthesis of dynamic scenes. Existing techniques already show impressive rendering quality but tend to focus on optimization within a single scene without leveraging prior knowledge. This limitation has been primarily attributed to the lack of datasets of dynamic scenes available for training and the diversity of scene dynamics. Our method FlowIBR circumvents these issues by integrating a neural image-based rendering method, pre-trained on a large corpus of widely available static scenes, with a per-scene optimized scene flow field. Utilizing this flow field, we bend the camera rays to counteract the scene dynamics, thereby presenting the dynamic scene as if it were static to the rendering network. The proposed method reduces per-scene optimization time by an order of magnitude, achieving comparable results to existing methods — all on a single consumer-grade GPU.

1. Introduction

Novel view synthesis for dynamic scenes allows for rendering views of an observed scene from new viewpoints, possibly also at new points in time. Recent methods [16, 17, 24, 26] already show impressive rendering qualities. Nevertheless, they suffer from long training times and show limitations for fast-changing scenes with sparse observations [10]. We assume that these limitations are partially due to the fact that these methods are only optimized per scene without exploiting any prior knowledge. Therefore, we present FlowIBR which combines a pre-trained generalizable novel view synthesis method [35] as a rendering backbone with a per-scene learned scene flow field.

For static scenes there is already a multitude of generalizable novel view synthesis methods [18, 30, 33, 35, 42] which are trained on multiple different scenes to learn how to aggregate information from prior observations to synthesize novel views. Importantly, generalizable methods are

trained on multiple scenes and can render novel views of previously unseen scenes *without* any scene-specific training. These methods often outperform per-scene optimized methods in terms of rendering quality, training times and demand for dense observation of the scene. However, due to the limited availability of datasets of dynamic scenes for training, such generalized methods cannot readily be extended to dynamic scenes.

To overcome this limitation, we build our method on Generalizable NeRF Transformer (GNT) [35], a generalizable view synthesis method which has been pre-trained on a large corpus of more easily obtainable static scenes. GNT utilizes neural image-based rendering (IBR) [42] which means synthesizing a novel view pixel-wise, by projecting camera rays as epipolar lines into neighbouring source views and then aggregating image information along them. However, in dynamic scenes, projections of independently moving scene content are likely displaced with respect to the epipolar lines. Therefore, we use a per-scene learned scene flow field to bend camera rays, so they follow the motion of the scene content for each time frame of the source observations as shown in Fig. 1 (top). The core optimization is thus simplified by shifting focus from jointly learning the complex interplay of scene geometry, color, and temporal changes to a separate step of learning the scene dynamics.

With this approach, we are able to reduce the necessary per-scene setup time to about 2 hours, an improvement by an order of magnitude compared to previous methods, while getting comparable rendering quality as illustrated in Fig. 1 (bottom). Additionally, this dynamics-focused optimization process allows us to create a training regime which enables optimizing the scene flow network on a single Nvidia 3080 RTX GPU. This stands in addition to the capability of concurrently fine-tuning the GNT, further enhancing the model’s performance. In summary, our contributions are:

- *Introducing FlowIBR*, a novel view synthesis method for dynamic scenes which combines a pre-trained neural image-based rendering method with a per-scene optimized scene flow field to decrease training time.

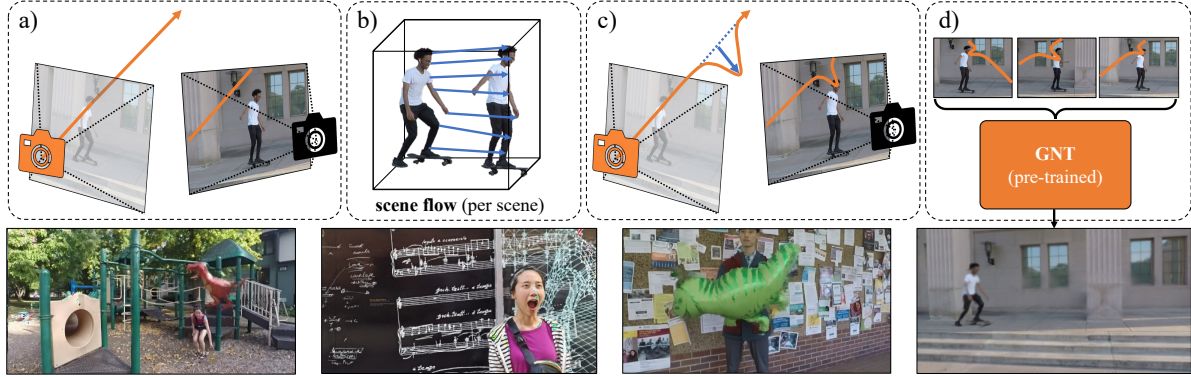


Figure 1. **Method overview (top) and synthesised images (bottom)** a) An image at an arbitrary position (orange camera) is synthesised based on existing observations (black camera), collected at different times. Problem: Due to the movement of the skater, the skater is not on the epipolar line of the camera ray, which is necessary for image-based rendering. b) We model scene motion using per-scene learned scene flow. c) Scene flow is used to compensate for the motion by adjusting the camera ray. d) GNT [35], a pre-trained neural IBR method for static scenes is used for image synthesis.

- *Presenting a dynamics-centred training regime* which allows for fast training of the proposed method on a single consumer-grade GPU.
- *Demonstrating the performance of FlowIBR* on the Nvidia Dynamic Scenes Dataset [44] showing competitive rendering quality despite significantly lower training times with respect to the state-of-the-art.

Code for the proposed method will be made available¹.

2. Related Work

Novel view synthesis for static scenes: Neural Radiance Fields (NeRFs) [20] and succeeding methods [1, 2, 21, 46] are able to synthesize photo-realistic images of a scene by modelling a continuous radiance and density function of an observed scene with a multi-layer perceptron (MLP). Image synthesis is then performed pixel-wise, by aggregating radiance and density along camera rays via volumetric rendering to a final pixel color.

Classical NeRF-based methods are optimized per scene without leveraging prior knowledge. In contrast, techniques for generalizable novel view synthesis are trained across multiple scenes, in order to allow for synthesis of novel views from sparsely observed scenes, unseen during training. Earlier methods such as pixelNeRF [45] and MVS-NeRF [4] have achieved this by deploying a generalizable NeRF conditioned on latent vectors extracted from the source observations.

Many of the current methods [6, 12, 18, 28, 33–35, 42] combine transformers [5, 39] with multi-view geometry. As proposed by IBRNet [42], this is realized by projecting points sampled along the camera ray for each pixel into

¹<https://flowibr.github.io>

the source observations. The information at these projected points is then extracted and subsequently aggregated into pixel color using transformers — often in combination with volumetric rendering. GNT [35] and a recent method from Du *et al.* [6] are fully transformer-based approaches, replacing the volumetric rendering, with a learned rendering.

Other approaches [8, 30, 31] learn the novel-view generation in an end-to-end fashion without relying on multi-view geometry. This can be beneficial to alleviate the need for exact camera poses [30, 31] or increase the generative capabilities to reduce the number of required observations [8].

Novel view synthesis for dynamic scenes: While early techniques required multi-view videos [15, 19, 41], current NeRF-based methods have demonstrated remarkable rendering capabilities from monocular videos. Methods such as D-NeRF [26], Nerfies [24] and HyperNeRF [25] learn a canonical NeRF representation at a fixed point in time, which is then warped by a learned motion field to other instances in time. This canonical scene representation serves as an anchor in time, accumulating the geometric and color information from source observations. NeRFPlayer [32] simplifies the training process further by decomposing the scene in static, dynamic and newly appearing scene content to decrease training and rendering times.

An alternative strategy involves learning a time-varying NeRF representation of the scene, exemplified by methods like NSFF [16] and DVS [9]. To address the ambiguity in observing non-rigid dynamic scenes with a single camera, these methods often employ additional regularization techniques. This includes incorporating data-driven supervision through monocular depth estimation [9, 16, 43, 44] (*e.g.* MiDaS [27]) or optical-flow estimation methods [7, 9, 16, 44] (*e.g.* RAFT [37]). Additionally, it is possible to add further

regularization, either enforcing consistent depths [7, 44] or smooth 3D scene flow [9, 16, 43].

A different line of work [14, 23] instantiates moving objects as separate bounded NeRFs inside a static environment NeRF, which are then rigidly moved between time-steps by learned transformations.

Similar to our approach, Fourier PlenOctree [41] utilizes generalizable novel view synthesis for dynamic scenes, but requires multi-view images. The concept of splitting the learning process — initially pre-training a static rendering framework and subsequently employing it to simplify the training of a dynamic approach — is also explored in DVS [9]. However, DVS optimizes both components only for a singular scene. A recent method DynIBaR [17] also utilizes neural IBR for novel view synthesis with techniques to address scene motion. The key distinction lies in DynIBaR being fully optimized on a single scene without utilizing pre-training, leading to long training times of up to 2 days on 8 GPUS.

3. Method

Problem formulation: Given a set of images $I_t \in \mathbb{R}^{H \times W \times 3}$ taken at discrete times $t \in \{1, \dots, T\}$ with known camera matrices $P_t \in \mathbb{R}^{3 \times 4}$, we denote the triplet (I_t, P_t, t) as an observation of the scene. We assume observations to be taken in constant time intervals Δt . The problem is now to synthesize a target view of the scene \tilde{I} from an *arbitrary* viewpoint defined by \tilde{P} and *continuous* time $\tilde{t} \in \mathbb{R}$, based on the set of available observations

$$O = \{(I_t, P_t, t)\}_{t=1}^T. \quad (1)$$

Overview: Our proposed method combines a pre-trained generalizable novel view synthesis method with a scene flow field which is learned per scene. In this section, we will review the rendering backbone used for static scenes, introduce the scene flow field model, describe the loss and regularization terms, and propose a training regime for fast training on a single GPU.

3.1. Pre-training on static scenes

For our rendering backbone we build upon Generalizable NeRF Transformer (GNT) [35], a transformer-based extension of IBRNet [42]. GNT is able to synthesize novel views of a *static* scene not seen during training, at an arbitrary target viewpoint. Novel view synthesis is performed pixel-wise in a two-stage process that involves two transformers.

View Transformer (VT): This initial stage encompasses aggregating information from source observations close to the target view. This is achieved by firstly encoding each source observation into a feature map using a U-Net [29] image encoder $F_t = \text{U-Net}(I_t)$. Using the camera matrix of the target view, a camera ray $r_{t,m}$ is cast from

the focal point e_t of the camera through the target pixel $m \in \{1, \dots, H \times W\}$ in ray direction $d_{t,m}$,

$$r_{t,m}(l) = e_t + l d_{t,m}. \quad (2)$$

Afterwards, N points $p_{t,m,n} = r_{t,m}(l_n)$ are sampled at different distances $l_n \in \mathbb{R}$ along this ray and projected onto each considered source observation. To simplify notation, we omit n and m indexes wherever possible. Consequently, these projected points are located on the respective epipolar lines, defined by the target pixel and the image planes of the source observations. Image features are extracted by interpolating the feature map at these projected points. For every individual point along the camera ray, the view transformer aggregates the associated image feature vectors through attention into a single feature vector, representing the scene content at that particular spatial location.

Ray Transformer (RT): This stage utilizes a ray transformer to conduct a learned ray-based rendering using the feature vectors created by the view transformer in the first stage. Using attention, the features along the ray are aggregated into a unified feature representation of that ray. A final multi-layer perceptron (MLP) is then applied to decode this ray feature vector, translating it into the corresponding RGB value for that particular ray.

Optimization: GNT is trained by using one of the observations as target, while employing the remaining observations as source observations. This is a technique commonly found in NeRFs [20] where a color prediction loss term

$$\mathcal{L}_{rgb} = \sum_m \|C_m - \hat{C}_m\|_2^2, \quad (3)$$

is applied to the final pixel color C_m and ground truth \hat{C}_m color of pixel m . In contrast to NeRF, GNT is trained for each training step on a different scene. This enables novel view synthesis for scenes not observed during training, without additional optimization. We select GNT as rendering backbone for our work, based on its state-of-the-art generalization capabilities and rendering quality. For more details about GNT, we refer to the original paper [35].

3.2. Scene flow field

Naively applying GNT to dynamic scenes after its static pre-training will yield insufficient results (see Sec. 4.3). GNT assumes a static setting, synthesizing target pixel colors from neural image features along source observations' epipolar lines. However, in dynamic scenes where each observation captures a distinct state, this method faces challenges due to potential misalignment between the information needed for the synthesized pixel and the expected epipolar line. Our goal is therefore to learn the underlying scene motion as scene flow fields [9, 16] in order to be able

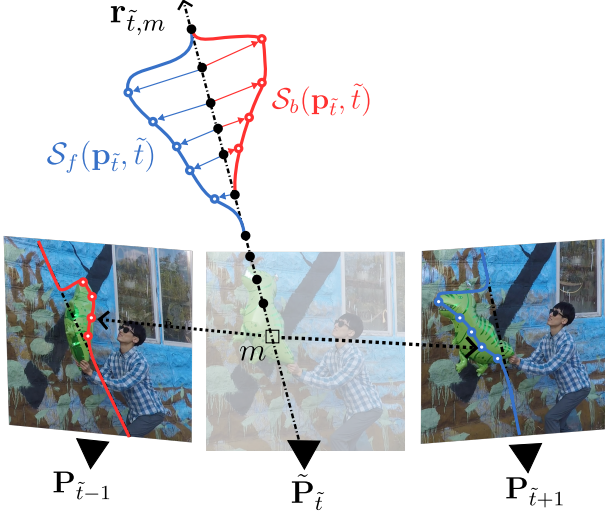


Figure 2. **Scene flow compensation** The scene flow (\mathcal{S}_f , \mathcal{S}_b) is used to adjust the ray $\mathbf{r}_{\tilde{t},m}$ from the target camera $\tilde{\mathbf{P}}_{\tilde{t}}$ through the current pixel m , so that it follows the motion of the balloon at the two adjacent times $\tilde{t}+1$ and $\tilde{t}-1$. This allows the projection of the ray on the source observations to contain the pixels corresponding to m , marked by arrows.

to realign the neural feature aggregation with the genuine image content.

We represent per-scene learned scene flow [9, 16] as a forward flow field

$$\mathcal{S}_f : (\mathbf{p}_t, t) \rightarrow \mathbf{s}_f \quad (4)$$

which maps each time $t \in \mathbb{R}$ and position $\mathbf{p}_t \in \mathbb{R}^3$ to a forward scene flow vector $\mathbf{s}_f \in \mathbb{R}^3$ and a backward flow field

$$\mathcal{S}_b : (\mathbf{p}_t, t) \rightarrow \mathbf{s}_b \quad (5)$$

which maps to a backward scene flow vector $\mathbf{s}_b \in \mathbb{R}^3$. These scene flow vectors can be used to displace a point from one time to an adjacent time step with

$$\mathbf{p}_{t \rightarrow t+1} = \mathbf{p}_t + \mathcal{S}_f(\mathbf{p}_t, t) \quad (6)$$

$$\mathbf{p}_{t \rightarrow t-1} = \mathbf{p}_t + \mathcal{S}_b(\mathbf{p}_t, t) \quad (7)$$

where we generally denote $\mathbf{p}_{t \rightarrow t+1}$ as the position \mathbf{p}_t adjusted to the next time $t+1$ and $\mathbf{p}_{t \rightarrow t-1}$ to the previous time $t-1$. The fields are represented by two different heads of the same MLP

$$\text{MLP}_{\theta} : (\psi(\mathbf{p}), t) \rightarrow (\mathbf{s}_f, \mathbf{s}_b). \quad (8)$$

Similar to NeRF [20], we encode the position with a sinusoidal encoding ψ [36, 39] to allow the network to capture high-frequency details. Through experimentation, we observed that restricting this encoding to the spatial dimensions, while leaving the temporal dimension unchanged, leads to the best performance.

3.3. Combined method

As illustrated in Fig. 2, we utilize the scene flow to adjust the 3D position of the points along the camera ray. This essentially *bends* the camera ray [26] — ensuring the ray points are projected to the parts of the image plane that contain dynamic content. Therefore, the camera rays will follow the moving scene content and thus prevent the GNT from being affected by scene motion, which allows for its use in dynamic scenes without any adjustments to its basic formulation.

For using more than just the two images closest to the target time \tilde{t} with GNT, it is necessary to estimate the scene flow $\mathbf{s}_{\tilde{t} \rightarrow t}$ from the target over a larger time window. This can be done with an iterative function evaluation of the scene flow network.

$$\mathbf{s}_{\tilde{t} \rightarrow t}(\mathbf{p}_{\tilde{t}}) = \begin{cases} \mathcal{S}_f(\mathbf{p}_{\tilde{t}}, \tilde{t}) + \mathcal{S}_{\tilde{t}+1 \rightarrow t}(\mathbf{p}_{\tilde{t}+1 \rightarrow t}) & , \tilde{t} < t \\ \mathcal{S}_b(\mathbf{p}_{\tilde{t}}, \tilde{t}) + \mathcal{S}_{\tilde{t}-1 \rightarrow t}(\mathbf{p}_{\tilde{t}-1 \rightarrow t}) & , \tilde{t} > t \\ \mathbf{0} & , \tilde{t} = t \end{cases} \quad (9)$$

This stays computationally feasible when selecting a sufficiently small MLP (e.g. 6 to 8 layers) for the scene flow, and basing the image synthesis process on images which are taken at temporally close to the target time $\mathcal{N}(\tilde{t}) \ni t$, to limit the number of times to adjust the rays for.

Rendering at continuous target times $\tilde{t} \in \mathbb{R}$ outside the intervals Δt , in which the scene has been observed, is facilitated by estimating the scene flow at the target time, and then linearly scaling the scene flow vectors, so they displace the points not over the full interval Δt but to the times of the next observations. Following this initial step, the motion adjustment can continue as previously described. More details on this can be found in the supplementary material.

3.4. Losses

The problem of learning a non-rigid dynamic scene from monocular observations is highly ambiguous. For example, an object that has seemingly grown from one observation to the next can either have changed its actual size or just moved towards the camera. This ambiguity creates the need for additional supervision and regularization besides the previously introduced \mathcal{L}_{rgb} loss. For the selection of losses that are used, we take inspiration from previous scene flow-based works [9, 16, 17].

Optical flow loss: Given the absence of a ground truth for the scene flow, the optical flow between the target image and source observations serves as an effective proxy which can be used for additional supervision. For this we use RAFT [37] to estimate the optical flow $\mathbf{o}_{\tilde{t} \rightarrow t}$ from the target image at time \tilde{t} to the used source observations at times t .

The optical flow estimate for each pixel is a 2D vector that represents the displacement to the corresponding pixel

location in a second image. We use this as supervision for the 3D scene flow, by taking the scene flow-adjusted points along the target ray, and projecting them onto the image plane of the observations. Then we calculate the difference between the pixel locations of the projected points and the pixel in the target image corresponding to the camera ray. This yields one pixel displacement vector per projected ray point. We use the attention weights of the ray transformer to estimate a weighted average $\mathbf{d}_{\tilde{t} \rightarrow t}$ of these. The optical flow loss is then calculated with the L1-norm between the optical flow $\mathbf{o}_{\tilde{t} \rightarrow t}$ estimated with RAFT and the weighted average $\mathbf{d}_{\tilde{t} \rightarrow t}$ of projected scene flow,

$$\mathcal{L}_{of} = \sum_{t \in \mathcal{N}(\tilde{t})} \|\mathbf{o}_{\tilde{t} \rightarrow t} - \mathbf{d}_{\tilde{t} \rightarrow t}\|_1. \quad (10)$$

This procedure is comparable to related methods [16, 17] which weigh pixel displacements with the opacity values of the NeRF representation. Due to noise in the optical flow, we only use \mathcal{L}_{of} to initialize the scene flow to a general direction, and linearly anneal its weight during training.

Cycle consistency regularization: To ensure that learned forward and backward scene flow are consistent to each other, we utilize *cycle consistency* regularization [9, 16, 17]. This means that the backwards scene flow of point \mathbf{p}_t should be equal to the forward scene flow of the displaced point $\mathbf{p}_{t \rightarrow t-1}$, but in the opposite direction,

$$\mathcal{L}_{cyc} = \sum_{t \in \mathcal{N}(\tilde{t})} \|\mathcal{S}_b(\mathbf{p}_t, t) + \mathcal{S}_f(\mathbf{p}_{t \rightarrow t-1}, t-1)\|_1 + \|\mathcal{S}_b(\mathbf{p}_{t \rightarrow t+1}, t+1) + \mathcal{S}_f(\mathbf{p}_t, t)\|_1. \quad (11)$$

Scene flow regularisation: We introduce three supplementary regularization terms to the scene flow, guiding it to learn anticipated properties of the inherent scene motion. For this we use the squared L2-norm between forward and backward scene flow as *temporal smoothness* regularization [9, 16, 17, 40]

$$\mathcal{L}_{temp} = \sum_{t \in \mathcal{N}(\tilde{t})} \|\mathcal{S}_f(\mathbf{p}_t, t) + \mathcal{S}_b(\mathbf{p}_t, t)\|_2^2 \quad (12)$$

which encourages the learning of a piece-wise linear solution. Additionally, we use the L1-norm on the predicted scene flow to support a generally *slow* scene flow, based on the common assumption, that most of the scene does not contain motion [9, 16, 38].

$$\mathcal{L}_{slow} = \sum_{t \in \mathcal{N}(\tilde{t})} \|\mathcal{S}_f(\mathbf{p}_t, t)\|_1 + \|\mathcal{S}_b(\mathbf{p}_t, t)\|_1 \quad (13)$$

Lastly, we encourage *spatial smoothness* so that narrow points along a ray are going to have similar scene flow [16,

17, 22]. For this, the difference between the forward and backward flows of neighbouring points $\mathbf{p}' \in \mathcal{N}(\mathbf{p})$ is weighted based on their distance

$$w(\mathbf{p}', \mathbf{p}) = \exp(-2\|\mathbf{p}' - \mathbf{p}\|_2^2). \quad (14)$$

The loss is then calculated on the L1-norm between the deviations in the flow.

$$\mathcal{L}_{spat} = \sum_{t \in \mathcal{N}(\tilde{t})} \sum_{\mathbf{p}' \in \mathcal{N}(\mathbf{p}_t)} (\|\mathcal{S}_f(\mathbf{p}_t, t) - \mathcal{S}_f(\mathbf{p}', t)\|_1 + \|\mathcal{S}_b(\mathbf{p}_t, t) - \mathcal{S}_b(\mathbf{p}', t)\|_1) \times w(\mathbf{p}', \mathbf{p}_t) \quad (15)$$

We summarize these losses to an aggregated regularization loss term

$$\mathcal{L}_{reg} = \mathcal{L}_{temp} + \mathcal{L}_{slow} + \mathcal{L}_{spat}. \quad (16)$$

Final loss: The final total loss is calculated by a weighted summation over the different loss terms

$$\mathcal{L} = \mathcal{L}_{rgb} + \alpha_{of}^k \mathcal{L}_{of} + \alpha_{cyc} \mathcal{L}_{cyc} + \alpha_{reg} \mathcal{L}_{reg}, \quad (17)$$

with α_{of}^k being linearly annealed over k steps of training.

3.5. Dynamics focused optimization

In the following, we will describe details of the process which will allow for optimization on a single GPU. For this we take advantage of the aspect that the optimization can focus on learning the scene flow, since the rendering has already been learned during pre-training. The general idea is to follow a coarse-to-fine approach [24] in learning scene flow, focusing on eliciting a coarse scene flow at the beginning, and then refining it as training time progresses.

Low-to-high number of source images: Training starts with a low number of source images to initially learn the scene flow between close time steps. Once the scene flow has started to emerge, we steadily increase the maximum number of source images at pre-defined steps to also learn the scene flow between more distant time steps. To keep a constant maximum GPU utilization, we adjust the ray batch size so that the total number of rays for all views remains constant, with a larger batch size in the beginning and then smaller batch sizes as the number of views increases.

Coarse-to-fine image resolutions: We observe that directly training the model on the original image resolution often leads to a zero collapse of the scene flow, i.e. the scene is incorrectly predicted to be fully static. To avoid falling into a trivial local minimum created by high-frequency details, we apply a coarse-to-fine scheme with the images originally subsampled by a factor of $f = 12$. The subsampling reduces the overall complexity of the correspondence

problem, and the batches of rays are more likely to cover also small dynamic areas. During training, we incrementally decrease the subsampling by reducing the factor by 2 to gradually refine the scene flow to represent the finer details of the underlying scene dynamics. This is analogue to coarse-to-fine refinement in optical flow methods [37]. Since we have experimentally observed that little is gained in quality by increasing the resolution up to the full resolution, we only increase it up to a factor of $f = 6$, which provides enough details to later render full-resolution images. Subsampling can be done offline and only takes a few seconds per scene, including subsampling of pre-calculated optical flow and motion masks.

Masked ray sampling: The regularization factors in \mathcal{L}_{reg} benefit learning of a near-zero scene flow in static regions of the scene. This allows us to focus the computational resources on the dynamic regions of the scene. We do so using binary motion masks $m: (x, y) \rightarrow \{0, 1\}$ that represent a coarse segmentation of dynamic regions in the image. Instead of sampling pixels uniformly across the image, we increase the sampling probability of pixels (x, y) in regions that are potentially dynamic, indicated by $m(x, y) = 1$.

Motion masks are estimated by using an off-the-shelf instance segmentation network [11]. Of the detected instances, we retain all potentially dynamic classes (e.g. person, car, skateboard) with a confidence above a threshold that is intentionally chosen to be small ($p = 0.1$), since discarding potentially dynamic content is worse than retaining static content. Overly small instances are removed via morphological opening, where we use a large dilation filter mask to create a wide boundary around the remaining segments which allows for learning a better transition from static to dynamic regions. Li *et al.* [16] also utilize dynamic masks, but employ them in a separate hard-mining stage in the beginning of the training to sample additional rays around dynamic regions.

Fine-tuning of rendering backbone: To further increase the visual rendering quality we fine-tune the rendering backbone on the current scene. This is possible with minimum computational overhead, since GNT is already part of the optimization loop of the scene flow network. We found this especially beneficial in combination with the optical flow loss, since the fine-tuning leads to refined attention weights of the ray transformer and therefore a more refined optical flow loss.

4. Experimental Results

In this section, we show the capabilities of our method, compare it to state-of-the-art baselines and ablations, as well as analyse the learned scene flow. For this we conduct

a comprehensive set of both quantitative and qualitative experiments.

4.1. Experimental setup

For the GNT backbone, we re-use the weights published by the authors. GNT was trained over 250,000 steps with 4096 rays per batch on several thousand scenes. Please refer to the corresponding paper [35], for more details. We use a six-layer deep MLP with width 256 as scene flow network, optimized with Adam [13] over 85k steps with a batch size of 512. For evaluation we render images based on 10 source observations. Further details on the used architecture and implementation can be found in the supplementary materials. Pre-calculating the optical flow, motion masks and subsampling takes on average 6:45min per scene on a Nvidia 3080 RTX GPU.

For the evaluation of the proposed method, FlowIBR, and the baselines, we use the Nvidia Dynamic Scenes Dataset [44]. The eight scenes in the dataset are observed by 12 static and synchronized cameras at 24 instances in time with fixed intervals. A moving camera is simulated by selecting one of the cameras for each timestep in a circular fashion to create the train set. Then for each training step, one camera position is selected to sample a ray batch, while the source observations are selected from the set of remaining images. During evaluation, observations present in the train set are kept as the source observations, while observations unseen during training are used as target images to estimate the metrics. The image dimensions are approximately Full HD (1920×1080) but vary from scene to scene with slight deviations in height.

For the quantitative evaluations we report Peak Signal-to-Noise Ratio (PSNR), Structural Similarity Index Measure (SSIM) [3] and Learned Perceptual Image Patch Similarity (LPIPS) [47]. In addition to evaluating these metrics over the entirety of the image, we report them also only considering image regions that exhibit dynamic content, leveraging the motion masks supplied with the dataset. To compute the dynamics-specific LPIPS, we adopt the masked LPIPS implementation from Li *et al.* [16].

4.2. Comparative evaluation

We benchmark FlowIBR against NSFF [16], DVS [9] and HyperNeRF [25], retraining each baseline using the configurations provided by the respective authors. For the most recent method, DynIBaR [17], we present the numbers earlier reported in the original publication. DynIBaR represents the current state-of-the-art in terms of rendering quality. However, it should be noted that it was trained with a minimum of 132 observations per scene, which is considerably more than the 24 observations used here. For a fair comparison in rendering time, we render images from all methods with 128 sampled points per camera ray. We use

Table 1. **Quantitative evaluation on Nvidia Dynamic Scenes [44]** We report PSNR, SSIM, LPIPS, and render time as average over all 8 scenes for the whole image as well as dynamic parts only. For NSFF we also report results on intermediate training checkpoints with the number of train steps in brackets. The added † for DynIBaR indicates that the results were taken from the original publication, which has been trained on Nvidia A100 GPUs. We see that FlowIBR (ours) has a significantly lower training time than the compared methods while obtaining competitive rendering quality.

Method	Train Time		Render Time		Full Image			Dynamic Regions		
	N _{GPU}	h	N _{GPU}	s/img	PSNR ↑	SSIM ↑	LPIPS ↓	PSNR ↑	SSIM ↑	LPIPS ↓
HyperNeRF	4	16:00	4	2.5	20.03	0.481	0.212	17.40	0.327	0.301
DVS	4	18:30	1	20.4	25.98	0.730	0.083	22.12	0.690	0.152
NSFF (50k)	4	3:30	1	6.2	26.70	0.633	0.092	21.06	0.633	0.183
NSFF (250k)	4	16:45	1	6.2	28.00	0.675	0.052	21.70	0.675	0.121
NSFF (1M)	4	58:15	1	6.2	28.20	0.681	0.044	21.75	0.681	0.103
DynIBaR [†]	8	48:00	1	20.0	30.92	0.958	0.027	24.32	0.827	0.061
FlowIBR (Ours)	1	2:15	1	25.1	26.88	0.692	0.096	21.12	0.680	0.201



Figure 3. **Qualitative evaluation on Nvidia Dynamic Scenes [44]** Renderings for each method retrained by us (HyperNeRF, DVS, NSFF). We can clearly see that that FlowIBR is able to synthesize novel views from previously unobserved viewpoints, with quality close to th ground truth (GT) image and to state-of-the-art methods.

images down-sampled by a factor of $f = 4$ to a resolution of (480×270) before using them for training or evaluation.

Qualitative results: Fig. 3 presents images rendered with our proposed method and the baselines that we retrained. FlowIBR demonstrates the capability to synthesize novel views from previously unobserved viewpoints, achieving a quality that is competitive with the state-of-the-art. Nevertheless, while accurately representing the scene, some rendered images exhibit motion blur in the dynamic regions.

Quantitative results: As the quantitative results in Tab. 1 indicate, FlowIBR performs competitively with respect to the baselines, but requires significantly shorter training time and only uses a single GPU. In terms of rendering quality, the results are comparable to those of NSFF, which requires an order of magnitude more GPU hours for training.

To better understand the relative performance of the methods, we limited NSFF to a more similar training budget and evaluated the method at different checkpoints. Our analysis suggests that this leads to a decline in NSFF’s performance, causing it to underperform in comparison to FlowIBR. The moderate rendering speed of our approach can be attributed to two primary factors. First, we employ a generalizable rendering backbone that, although highly versatile, has not been specifically optimized for speed. Second, our image-based rendering approach necessitates the projection of camera rays across all source observations, unlike NeRF-based methods that often render in a single forward pass.

4.3. Ablation study

We conduct an ablation study, summarized in Tab. 2, to analyze the contribution of the different parts of our methods. For this we compare the full model to ablations, each

Table 2. **Ablation study** Metrics are an average of results on the the *Balloon1*, *Truck2* and *DynamicFace* scenes. Best result is **bold** and second best underlined. We see that our full method outperforms all ablated versions, although some ablations show high performance in individual metrics.

Ablation	Full Image			Dynamic Regions		
	PSNR	SSIM	LPIPS	PSNR	SSIM	LPIPS
(1) default GNT	24.1	0.693	0.233	18.5	0.482	0.394
(2) $f = 4$	26.5	0.833	0.126	20.6	0.609	0.214
(3) $f = 12$	26.8	0.840	0.119	21.0	0.612	0.219
(4) \mathcal{L}_{of}	26.0	0.830	0.114	19.6	0.566	0.209
(5) \mathcal{L}_{cyc}	27.2	0.845	0.116	21.1	0.620	0.209
(6) \mathcal{L}_{reg}	<u>27.3</u>	0.844	0.120	21.1	0.659	0.200
(7) dyn. mask	<u>27.3</u>	0.851	0.103	21.4	0.630	0.194
(8) fine-tune	<u>27.3</u>	0.853	0.110	<u>21.6</u>	0.650	<u>0.197</u>
full	27.4	<u>0.852</u>	<u>0.109</u>	21.7	<u>0.651</u>	0.194

obtained by selectively omitting one component at a time. The components under scrutiny were: (1) only using GNT without the scene flow, (2-3) the coarse-to-fine instead of constant subsampling factor f , (4) the optical-flow loss \mathcal{L}_{of} , (5) the cycle loss \mathcal{L}_{cyc} , (6) the additional scene flow regularization losses $\mathcal{L}_{reg} = \mathcal{L}_{slow} + \mathcal{L}_{spat} + \mathcal{L}_{temp}$, (7) the usage of dynamic-static masks for ray sampling and (8) the fine-tuning of GNT. Despite some ablations showing similar performance, the full model was either best or second best on all metrics. Most importantly, the results show that the introduction of flow compensation substantially improves the image quality by 3.3 in PSNR for the whole image and 3.2 for the dynamic regions of the image.

4.4. Analysis of learned scene flow

To analyze the learned scene flow, we visualize the forward (s_f) and backward (s_b) scene flow for the rays of a selected reference view in Fig. 4. We project this flow onto the image plane and employ color coding, a common practice for optical flow methods. The flow is predominantly observed at pixels corresponding to the balloon, and the color-coded directions indicate a proper counter-clockwise movement, where s_f and s_b are nearly inverse to each other. This visualization illustrates the capability of FlowIBR in capturing nuanced scene dynamics.

Limitations: Since FlowIBR is initialized with optical flow, it inherits issues that complicate optical flow estimation, such as occlusions and undefined flow in large homogeneous areas. Long sequences can become challenging as a singular scene flow network, restricted by its finite capacity, must capture the entire flow. Future research could potentially address this limitation by adopting hybrid data structures such as Instant-NGP [21]. For scenes with fine scene motion, our method occasionally fails to converge,

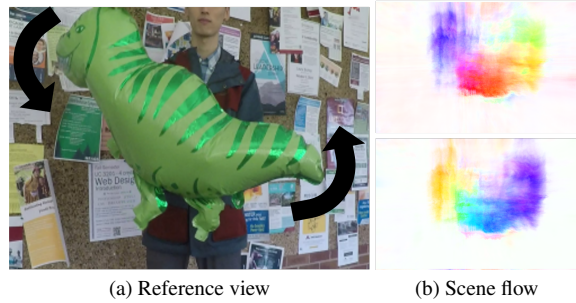


Figure 4. **Scene flow visualization** Projection of s_f (top) and s_b (bottom) onto the image plane. The arrows in the reference view show the true scene motion. Scene flow is visualized with hue indicating the direction and intensity the magnitude. Here our method correctly learned the rotating motion shown in the image.

instead learning a continuous near-zero scene flow. These issues can typically be solved through scene-specific parameter tuning or alternative network weight initialization.

5. Discussion and Conclusion

In this paper, we presented FlowIBR, a novel view synthesis method for dynamic scenes which utilizes a pre-trained rendering method, to decrease the necessary training time. The main challenge was circumventing the issue of lacking training data for novel view synthesis for dynamic scenes to utilize a pre-trained generalizable method. We solve this by employing a per-scene learned scene flow network, which is used to adjust the observations from different points in time, so they appear to be static to the pre-trained model. With this we can utilize a readily-available rendering backbone [35] for static scenes in the dynamic domain, allowing shorter training times and usage of a single consumer-grade GPU. We would like to address the moderate rendering speed of FlowIBR in future work, by creating a specialized rendering backbone which focuses even more on fast training and rendering.

Societal Impact: We anticipate several potential impacts of our proposed method, and similar methods, on society in the future. Primarily, we present a method to decrease the necessary training time for novel view synthesis methods for dynamic scenes and allow training on a single consumer-grade GPU which has the potential to democratize research capabilities, alleviating the dependency on specialized hardware. While our approach relies on the accumulated knowledge from pre-training, it is imperative to note that any biases present in the used datasets might propagate through our system. However, as the essence of our research is to synthesize views that are as faithful to the ground truth as possible, we are actively addressing this challenge to ensure accuracy and integrity of our results.

References

- [1] Jonathan T. Barron, Ben Mildenhall, Matthew Tancik, Peter Hedman, Ricardo Martin-Brualla, and Pratul P. Srinivasan. Mip-NeRF: A Multiscale Representation for Anti-Aliasing Neural Radiance Fields. In *IEEE/CVF International Conference on Computer Vision (ICCV)*, pages 5835–5844, 2021. [2](#)
- [2] Jonathan T. Barron, Ben Mildenhall, Dor Verbin, Pratul P. Srinivasan, and Peter Hedman. Mip-NeRF 360: Unbounded Anti-Aliased Neural Radiance Fields. In *IEEE/CVF Conference on Computer Vision and Pattern Recognition (CVPR)*, pages 5460–5469, 2022. [2](#)
- [3] Dominique Brunet, Edward R. Vrscay, and Zhou Wang. On the Mathematical Properties of the Structural Similarity Index. *IEEE Transactions on Image Processing*, 21(4):1488–1499, 2012. [6](#)
- [4] Anpei Chen, Zexiang Xu, Fuqiang Zhao, Xiaoshuai Zhang, Fanbo Xiang, Jingyi Yu, and Hao Su. MVNeRF: Fast Generalizable Radiance Field Reconstruction from Multi-View Stereo. In *IEEE/CVF International Conference on Computer Vision (ICCV)*, pages 14104–14113, 2021. [2](#)
- [5] Alexey Dosovitskiy, Lucas Beyer, Alexander Kolesnikov, Dirk Weissenborn, Xiaohua Zhai, Thomas Unterthiner, Mostafa Dehghani, Matthias Minderer, Georg Heigold, Sylvain Gelly, Jakob Uszkoreit, and Neil Houlsby. An Image is Worth 16x16 Words: Transformers for Image Recognition at Scale. In *International Conference on Learning Representations (ICLR)*, 2022. [2](#)
- [6] Yilun Du, Cameron Smith, Ayush Tewari, and Vincent Sitzmann. Learning To Render Novel Views From Wide-Baseline Stereo Pairs. In *IEEE/CVF Conference on Computer Vision and Pattern Recognition (CVPR)*, pages 4970–4980, 2023. [2](#)
- [7] Yilun Du, Yanan Zhang, Hong-Xing Yu, Joshua B. Tenenbaum, and Jiajun Wu. Neural Radiance Flow for 4D View Synthesis and Video Processing. In *IEEE/CVF International Conference on Computer Vision (ICCV)*, pages 14304–14314, 2021. [2](#), [3](#)
- [8] S. M. Ali Eslami, Danilo Jimenez Rezende, Frederic Besse, Fabio Viola, Ari S. Morcos, Marta Garnelo, Avraham Ruderman, Andrei A. Rusu, Ivo Danihelka, Karol Gregor, David P. Reichert, Lars Buesing, Theophane Weber, Oriol Vinyals, Dan Rosenbaum, Neil Rabinowitz, Helen King, Chloe Hillier, Matt Botvinick, Daan Wierstra, Koray Kavukcuoglu, and Demis Hassabis. Neural scene representation and rendering. *Science*, 360(6394):1204–1210, 2018. [2](#)
- [9] Chen Gao, Ayush Saraf, Johannes Kopf, and Jia-Bin Huang. Dynamic View Synthesis from Dynamic Monocular Video. In *IEEE/CVF International Conference on Computer Vision (ICCV)*, pages 5692–5701, 2021. [2](#), [3](#), [4](#), [5](#), [6](#)
- [10] Hang Gao, Ruilong Li, Shubham Tulsiani, Bryan Russell, and Angjoo Kanazawa. Monocular Dynamic View Synthesis: A Reality Check. In *Advances in Neural Information Processing Systems (NeurIPS)*, pages 33768–33780, 2022. [1](#)
- [11] Kaiming He, Georgia Gkioxari, Piotr Dollár, and Ross Girshick. Mask R-CNN. In *IEEE/CVF International Conference on Computer Vision (ICCV)*, pages 2980–2988, 2017. [6](#)
- [12] Mohammad Mahdi Johari, Yann Lepoittevin, and Francois Fleuret. GeoNeRF: Generalizing NeRF with Geometry Priors. In *IEEE/CVF Conference on Computer Vision and Pattern Recognition (CVPR)*, pages 18344–18347, 2022. [2](#)
- [13] Diederik P. Kingma and Jimmy Ba. Adam: A Method for Stochastic Optimization. In *International Conference on Learning Representations (ICLR)*, 2015. [6](#)
- [14] Abhijit Kundu, Kyle Genova, Xiaoqi Yin, Alireza Fathi, Caroline Pantofaru, Leonidas Guibas, Andrea Tagliasacchi, Frank Dellaert, and Thomas Funkhouser. Panoptic Neural Fields: A Semantic Object-Aware Neural Scene Representation. In *IEEE/CVF Conference on Computer Vision and Pattern Recognition (CVPR)*, pages 12861–12871, 2022. [3](#)
- [15] Tianye Li, Mira Slavcheva, Michael Zollhoefer, Simon Green, Christoph Lassner, Changil Kim, Tanner Schmidt, Steven Lovegrove, Michael Goesele, Richard Newcombe, and Zhaoyang Lv. Neural 3D Video Synthesis from Multi-view Video. In *IEEE/CVF Conference on Computer Vision and Pattern Recognition (CVPR)*, pages 5511–5521, 2022. [2](#)
- [16] Zhengqi Li, Simon Niklaus, Noah Snavely, and Oliver Wang. Neural Scene Flow Fields for Space-Time View Synthesis of Dynamic Scenes. In *IEEE/CVF Conference on Computer Vision and Pattern Recognition (CVPR)*, pages 6494–6504, 2021. [1](#), [2](#), [3](#), [4](#), [5](#), [6](#)
- [17] Zhengqi Li, Qianqian Wang, Forrester Cole, Richard Tucker, and Noah Snavely. DynIBaR: Neural Dynamic Image-Based Rendering. In *IEEE/CVF Conference on Computer Vision and Pattern Recognition (CVPR)*, pages 4273–4284, 2023. [1](#), [3](#), [4](#), [5](#), [6](#)
- [18] Yuan Liu, Sida Peng, Lingjie Liu, Qianqian Wang, Peng Wang, Christian Theobalt, Xiaowei Zhou, and Wenping Wang. Neural Rays for Occlusion-aware Image-based Rendering. In *IEEE/CVF Conference on Computer Vision and Pattern Recognition (CVPR)*, pages 7814–7823, 2022. [1](#), [2](#)
- [19] Stephen Lombardi, Tomas Simon, Jason Saragih, Gabriel Schwartz, Andreas Lehrmann, and Yaser Sheikh. Neural volumes: learning dynamic renderable volumes from images. *ACM Transactions on Graphics*, 38(4):65:1–65:14, 2019. [2](#)
- [20] Ben Mildenhall, Pratul P. Srinivasan, Matthew Tancik, Jonathan T. Barron, Ravi Ramamoorthi, and Ren Ng. NeRF: Representing Scenes as Neural Radiance Fields for View Synthesis. In *European Conference on Computer Vision (ECCV)*, pages 405–421, 2020. [2](#), [3](#), [4](#)
- [21] Thomas Müller, Alex Evans, Christoph Schied, and Alexander Keller. Instant neural graphics primitives with a multiresolution hash encoding. *ACM Transactions on Graphics*, 41(4):1–15, 2022. [2](#), [8](#)
- [22] Richard A. Newcombe, Dieter Fox, and Steven M. Seitz. DynamicFusion: Reconstruction and tracking of non-rigid scenes in real-time. In *IEEE/CVF Conference on Computer Vision and Pattern Recognition (CVPR)*, pages 343–352, 2015. [5](#)
- [23] Julian Ost, Fahim Mannan, Nils Thuerey, Julian Knodt, and Felix Heide. Neural Scene Graphs for Dynamic Scenes. In *IEEE/CVF Conference on Computer Vision and Pattern Recognition (CVPR)*, pages 2855–2864, 2021. [3](#)

- [24] Keunhong Park, Utkarsh Sinha, Jonathan T. Barron, Sofien Bouaziz, Dan B Goldman, Steven M. Seitz, and Ricardo Martin-Brualla. Nerfies: Deformable Neural Radiance Fields. In *IEEE/CVF International Conference on Computer Vision (ICCV)*, pages 5845–5854, 2021. 1, 2, 5
- [25] Keunhong Park, Utkarsh Sinha, Peter Hedman, Jonathan T. Barron, Sofien Bouaziz, Dan B Goldman, Ricardo Martin-Brualla, and Steven M. Seitz. HyperNeRF: a higher-dimensional representation for topologically varying neural radiance fields. *ACM Transactions on Graphics*, 40(6):1–12, 2021. 2, 6
- [26] Albert Pumarola, Enric Corona, Gerard Pons-Moll, and Francesc Moreno-Noguer. D-NeRF: Neural Radiance Fields for Dynamic Scenes. In *IEEE/CVF Conference on Computer Vision and Pattern Recognition (CVPR)*, pages 10313–10322, 2021. 1, 2, 4
- [27] Rene Ranftl, Katrin Lasinger, David Hafner, Konrad Schindler, and Vladlen Koltun. Towards Robust Monocular Depth Estimation: Mixing Datasets for Zero-Shot Cross-Dataset Transfer. *IEEE Transactions on Pattern Analysis and Machine Intelligence*, 44(3):1623–1637, 2022. 2
- [28] Jeremy Reizenstein, Roman Shapovalov, Philipp Henzler, Luca Sbordone, Patrick Labatut, and David Novotny. Common Objects in 3D: Large-Scale Learning and Evaluation of Real-life 3D Category Reconstruction. In *IEEE/CVF International Conference on Computer Vision (ICCV)*, pages 10881–10891, 2021. 2
- [29] Olaf Ronneberger, Philipp Fischer, and Thomas Brox. U-Net: Convolutional Networks for Biomedical Image Segmentation. In *Medical Image Computing and Computer-Assisted Intervention (MICCAI 2015)*, pages 234–241, 2015. 3
- [30] Mehdi S.M. Sajjadi, Henning Meyer, Etienne Pot, Urs Bergmann, Klaus Greff, Noha Radwan, Suhani Vora, Mario Lucic, Daniel Duckworth, Alexey Dosovitskiy, Jakob Uszkoreit, Thomas Funkhouser, and Andrea Tagliasacchi. Scene Representation Transformer: Geometry-Free Novel View Synthesis Through Set-Latent Scene Representations. In *IEEE/CVF Conference on Computer Vision and Pattern Recognition (CVPR)*, pages 6219–6228, 2022. 1, 2
- [31] Mehdi S. M. Sajjadi, Aravindh Mahendran, Thomas Kipf, Etienne Pot, Daniel Duckworth, Mario Lucic, and Klaus Greff. RUST: Latent Neural Scene Representations from Unposed Imagery. In *IEEE/CVF Conference on Computer Vision and Pattern Recognition (CVPR)*, pages 17297–17306, 2023. 2
- [32] Liangchen Song, Anpei Chen, Zhong Li, Zhang Chen, Lele Chen, Junsong Yuan, Yi Xu, and Andreas Geiger. NeRF-Player: A Streamable Dynamic Scene Representation with Decomposed Neural Radiance Fields. *IEEE Transactions on Visualization and Computer Graphics*, 29(5):2732–2742, 2023. 2
- [33] Mohammed Suhail, Carlos Esteves, Leonid Sigal, and Ameesh Makadia. Generalizable Patch-Based Neural Rendering. In *European Conference on Computer Vision (ECCV)*, pages 156–174, 2022. 1, 2
- [34] Mohammed Suhail, Carlos Esteves, Leonid Sigal, and Ameesh Makadia. Light Field Neural Rendering. In *IEEE/CVF Conference on Computer Vision and Pattern Recognition (CVPR)*, pages 8259–8269, 2022. 2
- [35] Mukund Varma T, Peihao Wang, Xuxi Chen, Tianlong Chen, Subhashini Venugopalan, and Zhangyang Wang. Is Attention All That NeRF Needs? In *International Conference on Learning Representations (ICLR)*, 2023. 1, 2, 3, 6, 8
- [36] Matthew Tancik, Pratul Srinivasan, Ben Mildenhall, Sara Fridovich-Keil, Nithin Raghavan, Utkarsh Singhal, Ravi Ramamoorthi, Jonathan Barron, and Ren Ng. Fourier Features Let Networks Learn High Frequency Functions in Low Dimensional Domains. In *Advances in Neural Information Processing Systems (NeurIPS)*, pages 7537–7547, 2020. 4
- [37] Zachary Teed and Jia Deng. RAFT: Recurrent All-Pairs Field Transforms for Optical Flow. In *European Conference on Computer Vision (ECCV)*, pages 402–419, 2020. 2, 4, 6
- [38] J. Valmadre and S. Lucey. General trajectory prior for Non-Rigid reconstruction. In *IEEE Conference on Computer Vision and Pattern Recognition (CVPR)*, pages 1394–1401, 2012. 5
- [39] Ashish Vaswani, Noam Shazeer, Niki Parmar, Jakob Uszkoreit, Llion Jones, Aidan N Gomez, Łukasz Kaiser, and Illia Polosukhin. Attention is All you Need. In *Advances in Neural Information Processing Systems (NeurIPS)*, pages 6000–6010, 2017. 2, 4
- [40] Minh Vo, Srinivasa G. Narasimhan, and Yaser Sheikh. Spatiotemporal Bundle Adjustment for Dynamic 3D Reconstruction. In *IEEE/CVF Conference on Computer Vision and Pattern Recognition (CVPR)*, pages 1710–1718, 2016. 5
- [41] Liao Wang, Jiakai Zhang, Xinhang Liu, Fuqiang Zhao, Yan-shun Zhang, Yingliang Zhang, Minve Wu, Jingyi Yu, and Lan Xu. Fourier PlenOctrees for Dynamic Radiance Field Rendering in Real-time. In *IEEE/CVF Conference on Computer Vision and Pattern Recognition (CVPR)*, pages 13514–13524, 2022. 2, 3
- [42] Qianqian Wang, Zhicheng Wang, Kyle Genova, Pratul Srinivasan, Howard Zhou, Jonathan T. Barron, Ricardo Martin-Brualla, Noah Snavely, and Thomas Funkhouser. IBRNet: Learning Multi-View Image-Based Rendering. In *IEEE/CVF Conference on Computer Vision and Pattern Recognition (CVPR)*, pages 4688–4697, 2021. 1, 2, 3
- [43] Wenqi Xian, Jia-Bin Huang, Johannes Kopf, and Changil Kim. Space-time Neural Irradiance Fields for Free-Viewpoint Video. In *IEEE/CVF Conference on Computer Vision and Pattern Recognition (CVPR)*, pages 9416–9426, 2021. 2, 3
- [44] Jae Shin Yoon, Kihwan Kim, Orazio Gallo, Hyun Soo Park, and Jan Kautz. Novel View Synthesis of Dynamic Scenes With Globally Coherent Depths From a Monocular Camera. In *IEEE/CVF Conference on Computer Vision and Pattern Recognition (CVPR)*, pages 5335–5344, 2020. 2, 3, 6, 7
- [45] Alex Yu, Vickie Ye, Matthew Tancik, and Angjoo Kanazawa. pixelNeRF: Neural Radiance Fields from One or Few Images. In *IEEE/CVF Conference on Computer Vision and Pattern Recognition (CVPR)*, pages 4576–4585, 2021. 2
- [46] Kai Zhang, Gernot Riegler, Noah Snavely, and Vladlen Koltun. NeRF++: Analyzing and Improving Neural Radiance Fields. *arXiv preprint*, arXiv:2010.07492, 2020. 2

- [47] Richard Zhang, Phillip Isola, Alexei A. Efros, Eli Shechtman, and Oliver Wang. The Unreasonable Effectiveness of Deep Features as a Perceptual Metric. In *2018 IEEE/CVF Conference on Computer Vision and Pattern Recognition*, pages 586–595, 2018. [6](#)

FlowIBR: Leveraging Pre-Training for Efficient Neural Image-Based Rendering of Dynamic Scenes

Supplementary Material

1. Network architecture

The scene flow network is implemented as a six layer multi-layer perceptron (MLP) with a skip connection from the input to the third layer, which is displayed in Fig. 1. The activation function is ReLU. For being applicable to general scenes, FlowIBR does not utilize normalized device coordinates (NDC) which are in the range $[0, 1]$, but rather unbounded cartesian coordinates. Therefore, the last layer does not have an activation function. NDCs limits a method to forward facing scenes, but are common in NeRF based methods where the datasets often fulfill this criterion. For the sinusoidal encoding [2, 4, 5]

$$\psi(\mathbf{p}_t) = (\mathbf{p}_t, \sin(2^0\pi\mathbf{p}_t), \cos(2^0\pi\mathbf{p}_t), \dots, \sin(2^{L-1}\pi\mathbf{p}_t), \cos(2^{L-1}\pi\mathbf{p}_t)) \quad (1)$$

the number of frequencies is selected to be $L = 10$ for scenes with fine details, such as people waving their arms, and $L = 8$ for less detailed motions, such as a truck moving forward. The network does not use batch normalization, dropout or any other regularization not discussed in this paper.

2. Optimization

The network is trained over 85k steps with a batch size of 1024. Higher batch sizes are limited by the imposed restriction of being able to train on a single GPU, lower batch sizes lead to underfitting of the scene flow. Adam [1] is used as optimizer for training with $\beta_1 = 0.9$, $\beta_2 = 0.999$ and $\epsilon = 10^{-8}$. We experimented with a higher value for β_1 to increase the momentum in the running average to compensate for only having one observation per training step, but found results to be worse. The learning rate is $l_{flow} \in [10^{-3}, 10^{-4}]$ for the flow network and $l_{GNT} \in [10^{-6}, 10^{-8}]$ for the GNT [4] fine-tuning. We only fine-tune the GNT transformer weights, while keeping the image encoder frozen. Every 20k steps, the learning rate is decreased by 50%. The weights for the regularization terms are as follows: $\alpha_{cyc} = 0.02$, $\alpha_{slow} = 0.01$, $\alpha_{spat} = 0.05$, $\alpha_{spat} = 0.1$, $\alpha_{of}^k = 0.005$, with α_{of}^k being linearly annealed over 40k steps. The low factor for the optical-flow is selected to compensate for the optical flow loss term being about 100 times higher than the other losses.

3. Depth estimation

Using the attention weights of the ray transformer, it is possible to infer a depth value for each pixel in the estimated

image [4]. This is possible, since the ray transformer will put the most attention on the points sampled along the ray that are contributing the most to the final pixel color, which most likely corresponds to a solid surface. Therefore, depth can be estimated by weighting the distance of points along the ray by the attention weights the ray transformer puts on them. An example for this is shown in Fig. 2. In future work, this could allow for additional supervision with monocular depth estimation methods such as MiDaS [3]

4. Rendering at non-observed times

Rendering at continuous target times $\tilde{t} \in \mathbb{R}$ outside the intervals Δt in which the scene has been observed, is facilitated by initiating the motion adjustment by first adjusting the continuous times to the two neighbouring observations times, with

$$\tilde{t}_b(\tilde{t}) = \left\lfloor \frac{\tilde{t}}{\Delta t} \right\rfloor \quad (2)$$

as the previous neighbour, and

$$\tilde{t}_f(\tilde{t}) = \left\lceil \frac{\tilde{t}}{\Delta t} \right\rceil \quad (3)$$

as the succeeding neighbour. With $\lfloor \cdot \rfloor$ we denote the floor operator and with $\lceil \cdot \rceil$ the ceiling operator.

Using a scaling factor for the scene flow, given by:

$$\delta_b(\tilde{t}) = \frac{\tilde{t}}{\Delta t} - \tilde{t}_b, \quad (4)$$

for the backward floor, and respectively:

$$\delta_f(\tilde{t}) = \tilde{t}_f - \frac{\tilde{t}}{\Delta t}, \quad (5)$$

for the forward flow to then displace the ray points from the target time \tilde{t} to the adjacent discrete observation times. For instance, forward time adjustments can be represented as:

$$\mathbf{p}_{\tilde{t} \rightarrow \tilde{t}_f} = \mathbf{p}_{\tilde{t}} + \delta_f(\tilde{t})\mathcal{S}_f(\mathbf{p}_{\tilde{t}}, \tilde{t}). \quad (6)$$

Following this initial step, the motion adjustment can continue as described for discrete times.

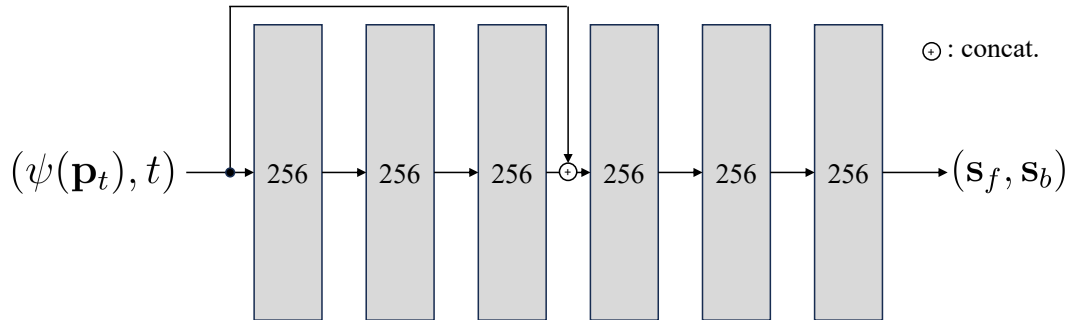


Figure 1. Scene flow field architecture



Figure 2. **Depth estimation.** After rendering the target image (left), the distances of points along the camera ray are weighted by the corresponding ray attention weights and then summed to a depth estimate (right).

References

- [1] Diederik P. Kingma and Jimmy Ba. Adam: A Method for Stochastic Optimization. In *International Conference on Learning Representations (ICLR)*, 2015. 1
- [2] Ben Mildenhall, Pratul P. Srinivasan, Matthew Tancik, Jonathan T. Barron, Ravi Ramamoorthi, and Ren Ng. NeRF: Representing Scenes as Neural Radiance Fields for View Synthesis. In *European Conference on Computer Vision (ECCV)*, pages 405–421, 2020. 1
- [3] Rene Ranftl, Katrin Lasinger, David Hafner, Konrad Schindler, and Vladlen Koltun. Towards Robust Monocular Depth Estimation: Mixing Datasets for Zero-Shot Cross-Dataset Transfer. *IEEE Transactions on Pattern Analysis and Machine Intelligence*, 44(3):1623–1637, 2022. 1
- [4] Mukund Varma T, Peihao Wang, Xuxi Chen, Tianlong Chen, Subhashini Venugopalan, and Zhangyang Wang. Is Attention All That NeRF Needs? In *International Conference on Learning Representations (ICLR)*, 2023. 1
- [5] Matthew Tancik, Pratul Srinivasan, Ben Mildenhall, Sara Fridovich-Keil, Nithin Raghavan, Utkarsh Singhal, Ravi Ramamoorthi, Jonathan Barron, and Ren Ng. Fourier Features Let Networks Learn High Frequency Functions in Low Dimensional Domains. In *Advances in Neural Information Processing Systems (NeurIPS)*, pages 7537–7547, 2020. 1